Power Electronic Systems
Laboratory

Proceedings of the 12th International Symposium on Linear Drives for Industry Applications (LDIA 2019), Neuchatel, Switzerland, July 1-3, 2019

Design and Comparison of Permanent Magnet Self-Bearing Linear-Rotary Actuators

S. Miric,
D. Bortis,
J. W. Kolar

Eidgenössische Technische Hochschule Zürich
Swiss Federal Institute of Technology Zurich

Design and Comparison of Permanent Magnet Self-Bearing Linear-Rotary Actuators

Spasoje Mirić, Dominik Bortis and Johann Walter Kolar
Power Electronic Systems Laboratory
ETH Zurich
Zurich, Switzerland
Email: miric@lem.ee.ethz.ch

***Abstract*—Linear-rotary actuators (LiRAs) are electric machines that can perform linear and rotary movements. They are used in many different applications, for example, for pick-and-place robots, in packaging or sorting lines, or as gearbox actuators. A linear-rotary movement can be obtained with various combinations of linear and rotary machines, whereas depending on the specifications of the underlying application the most suitable actuator arrangement has to be identified. In order to simplify the selection of the appropriate actuator configuration, this paper first gives an overview of possible realization concepts of linear-rotary actuators, which are also suitable to implement magnetic bearings (MB). Afterwards, fundamental scaling laws concerning achievable axial forces and torques of linear and rotary machines with interior and exterior rotor arrangement are derived, enabling a qualitative comparison in order to figure out the most suitable actuator concept. In this context, it is important that the derivation also considers the machine-internal heat flow and the heat dissipation to the ambient, which finally leads to a maximum current density depending on the selected topology. All findings are verified by finite element method simulations. In order to show the applicability of the derived scaling laws, a design example is discussed.**

***Index Terms*—Current density, axial force, torque, linear-rotary actuators, tubular actuators, magnetic bearings, self-bearing.**

I. Introduction

Linear-Rotary Actuators (LiRAs) are used in many different industries and application areas, for example, in electronics and semiconductor manufacturing industries in pick-and-place robots [1], [2], or in industries such as aerospace or automotive [3]–[5], food or pharmaceutical. Since LiRAs are used in so many different application areas, they have to meet different torque and/or force requirements, while also a given axial stroke has to be achieved. Consequently, choosing the most suitable actuator for given application specifications is not an easy task. Therefore, in this paper, torque and force scaling laws that give a quick and clear performance overview of different actuator arrangements are derived and verified with finite element method (FEM) simulations. Compared to scaling law derivations already done in literature [6], also thermal aspects are considered, which show to have a significant influence onto the optimal actuator geometry.

This paper focuses on permanent magnet (PM) LiRAs, as in general they have the highest power densities [7], but the derived scaling laws can also be applied to reluctance, flux switching or induction machines [2]. Besides the machine type, LiRAs can be realized in many different combinations of individual actuators, whereby also the coupling of the machines can be versatile, e.g. a parallel or series mechanical coupling, a magnetic coupling (e.g. checkerboard actuator [8]) or a double stator configuration [9], [10] can be used. However, as the LiRA with parallel mechanical coupling has a mechanical connection of the linear and rotary actuators [7], with independent rotors (also called 'movers' or 'sliders'), it is not further considered in this work, since it would result in a bulkier and less robust design with lower acceleration performances due to higher moving mass and moment of inertia.

This work was supported by ETH Research Grant ETH-13 16-2.

978-1-5386-5804-8/19/$31.00 ©2019 IEEE

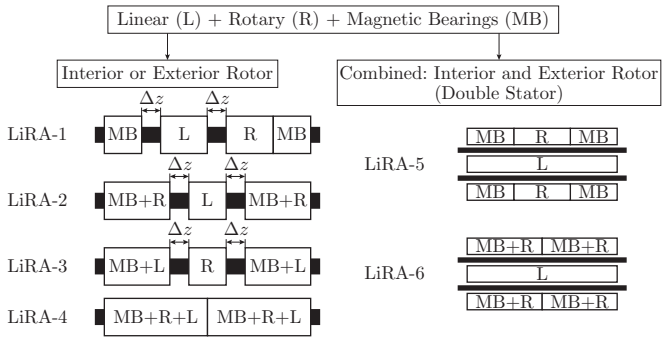

Fig. 1: Possible axial combinations of linear machines (L), rotary machines (R) and magnetic bearings (MB) to realize a self-bearing linear-rotary actuator. The possible combinations can be divided into two groups, where the first group uses either only interior or exterior rotor, while the second group is using a combined rotor, i.e. a double stator machine.

Another important aspect in LiRAs are the bearings. Most of the LiRAs use mechanical bearings, either ball or slider bearings. Besides their high stiffness and simplicity, both of those feature drawbacks, such as the need for lubrication and the particle generation. This is mainly a problem in applications where a high purity is required, e.g. in clean room applications. As an alternative, air bearings could be used, but they require a pressurized air supply and the operation in low pressure environments is prohibited. Accordingly, the mentioned issues can only be solved by magnetic bearings (MBs), which are gaining more and more attention in tubular linear and linear-rotary actuators [11]–[13].

This paper first summarizes possible options to realize a LiRA with MBs, and afterwards provides initial design considerations in terms of general scaling laws of electric machines that would help a potential designer to chose a topology suitable to the desired application. In contrast to the existing literature, the derived scaling laws also consider the machine-internal heat flow and the heat transfer to the ambient. Furthermore, the general scaling laws are applicable to any kind of electric machine and are also verified by FEM simulation.

II. Actuator Topology Concepts

Depending on the application specifications, the LiRA with magnetic bearings (MB) can be built with different combinations of linear (L) and rotary (R) machines, as shown in **Fig. 1**. The considered actuators are divided into two groups, the first that features only an axial stator displacement of the different machines (i.e. linear, rotary or magnetic bearing) with either all interior rotor (cf. **Fig. 2(a)**) or all exterior rotor arrangements (cf. **Fig. 2(b)**), and the second group featuring a combined stator arrangement, i.e. a double stator LiRA (cf. **Fig. 2(c)**).

As can be noticed, for all possible LiRA arrangements always two independent magnetic bearings (MB) on each axial end are

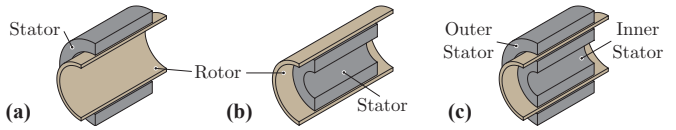

Fig. 2: Radial actuator arrangements: **(a)** interior rotor, **(b)** exterior rotor and **(c)** combined rotor featuring two radially displaced stators, also known in literature as double stator motor (cf. [14]).

required, such that rotor tilting can be controlled. Furthermore, depending on the degree of integration, the magnetic bearing can be either realized as an independent machine with separate stator (cf. LiRA-1 in **Fig. 1**) or can be integrated either into the rotary machine, i.e. a self-bearing rotary machine (MB+R) [15], or into the linear (L) machine (cf. LiRA-2 and LiRA-3 in **Fig. 1**), while a full integration of all three machines into a single machine is also possible (cf. LiRA-4 in **Fig. 1**). The realization options of these machines are shown in **Fig. 3**, where in the first row the different rotor's permanent magnet arrangements and in the second row the corresponding stator's winding configurations are given. As can be noticed, a rotary machine realized with a R-Rotor and R-Stator can also perform self-bearing (MB+R), while a linear machine (L) with L-Rotor and L-Stator doesn't feature magnetic levitation. Hence, the integration of the magnetic bearing into a rotary machine (MB+R) is easier to realize compared to the integration of the MB into a linear machine (MB+L). In order to achieve self-bearing and linear movement in one machine, the L-Rotor must be combined with a CB-Rotor ('Checkerboard-Rotor', cf. [8]), as done in [13]. A further option to realize either a self-bearing rotary machine (MB+R) or a linear machine (L), is to use a S-Rotor ('Square-Magnet-Rotor', cf. [10]) with either a R-Stator or an L-Stator. Finally, to fully integrate all features into a single machine (MB+R+L), a CB-Rotor with the CB-Stator is needed. It should be noted that the same integration concepts (except the full integration) can also be applied to the double stator LiRA (cf. LiRA-5 and LiRA-6 in **Fig. 1**) and that the functionalities of the inner and outer stator can also be exchanged, i.e. the linear machine (L) would then be the outer actuator and the magnetic bearing (MB) together with the rotary machine (R) would be the inner actuator. Another aspect in LiRAs is the maximum axial stroke z_{stroke} that can be achieved with the selected machine arrangement. First of all, it has to be considered that the rotor or mover should be longer than the total stator length for at least z_{stroke}, such that a constant interaction between the stator and the rotor is obtained. Furthermore, it has to be considered that depending on the selected stator and rotor arrangement, a certain distance Δz between the different stators is needed, which in case of an independent linear (L) or rotary (R) machine would have to be $\Delta z = z_{\text{stroke}}$ (cf. LiRA-1 to LiRA-3 in **Fig. 1**), while for a fully integrated checkerboard machine or a double-stator machine no distance between the stators is needed, i.e. $\Delta z = 0$ (cf. LiRA-4 to LiRA-6 in **Fig. 1**). Indeed, LiRAs with an S- or CB-Rotor can be realized with $\Delta z = 0$, however, as will be shown in the following section, they also feature lower torque and force densities due to the inherently lower flux linkage of the S-Rotor [10] or the larger end windings of the CB-Stator [16], and therefore finally result in a larger machine volume to achieve the same force and torque performances. For sake of completeness, the LiRA assemblies from **Fig. 1** are listed in **Tab. I** for the different rotor and stator realizations given in **Fig. 3** and it is shown whether a distance Δz between the stators is needed or not.

III. Scaling Laws

In this section, the scaling laws for the achievable torque and the thrust force of the *Interior Rotor* and *Exterior Rotor* actuator arrangements are derived. In contrast to other literature [6], the current density amplitude $\hat{J}$ is calculated from the thermal

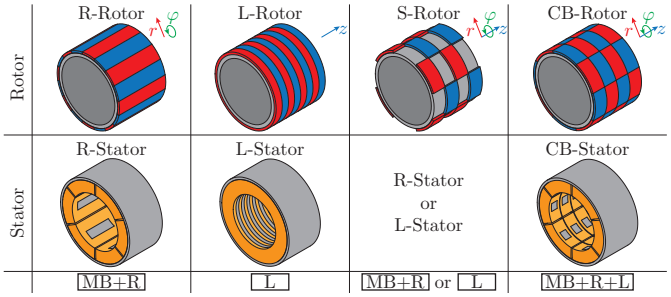

Fig. 3: Viable rotor and stator realization options that can be used for the LiRA design, i.e. R-Rotor and R-Stator to realize a rotary machine which also can perform self-bearing, L-Rotor and L-Stator for the linear machine, S-Rotor ('Square-Magnet-Rotor', cf. [10]) with either R-Stator or L-Stator to realize either a self-bearing rotary machine or a linear machine, and CB-Rotor ('Checkerboard-Rotor', cf. [8]) with CB-Stator to realize a fully integrated machine featuring the linear and rotary movement as well as the magnetic bearing. Furthermore, the L-Rotor can also be in combination with the CB-Stator in order to realize a self-bearing linear machine [13]. These realization concepts are only shown for the interior rotor actuator, but the same winding configuration and the permanent magnet arrangement can also be applied for the exterior rotor actuator.

TABLE I: Overview of the LiRA assemblies.

Rotor	Stator	Δz
LiRA-1: (MB, L, R, MB)		
(R, L, R, R)	(R, L, R, R)	z_{stroke}
(S, S, S, S)	(R, L, R, R)	0
LiRA-2: (MB+R, L, MB+R)		
(R, L, R)	(R, L, R)	z_{stroke}
(S, S, S)	(R, L, R)	0
LiRA-3: (MB+L, R, MB+L)		
(L, R, L)	(CB, R, CB)	z_{stroke}
(S, S, S)	(CB, R, CB)	0
LiRA-4: (MB+R+L, MB+R+L)		
(CB, CB)	(CB,CB)	0
LiRA-5: (MB, R, MB / L)		
(R, R, R / L)	(R, R, R / L)	0
(S, S, S / S)	(R, R, R / L)	0
LiRA-6: (MB+R, MB+R / L)		
(R, R / L)	(R, R / L)	0
(S, S / S)	(R, R / L)	0

(cooling) considerations, which have a significant influence on the achievable torques and forces. The scaling laws are verified with FEM simulations for the stator and rotor realizations shown in **Fig. 3**. The considered parameters are given in **Tab. II**.

Furthermore, it is assumed that the thickness of the rotor, the stator back iron, the permanent magnet, and the air gap are identical for all machines and compared to the outer dimensions, i.e. the inner and outer radii r and R as well as the length L of stator, are negligible. Moreover, also the air gap flux density B_{ag} is fixed to a constant value for all machines.

In [6], the current density amplitude $\hat{J}$ is assumed to be constant. This work extends the approach and $\hat{J}$ is calculated from the thermal (cooling) considerations, which, as shown later, significantly influence the achievable torque and force.

A. Interior Rotor

1) Torque Scaling Law: According to the fundamental expression for 3-phase electric machines, the torque magnitude T_{int} is proportional to the product of the flux linkage $\hat{\Psi}$ and the current amplitude $\hat{I}_{\text{int}}$ of the symmetric 3-phase winding system, i.e. $T_{\text{int}} \sim \hat{\Psi}\hat{I}_{\text{int}}$. The flux linkage $\hat{\Psi}$ is the total flux linked with the N turns of the stator winding. Therefore, the flux $\hat{\Phi}$ that penetrates the stator from the air gap is N times smaller,

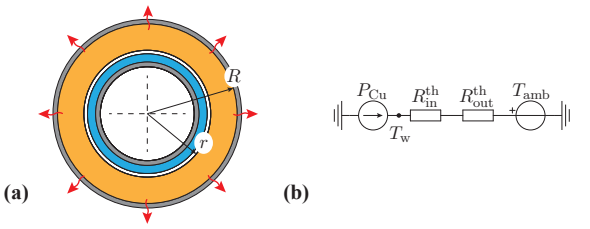

Fig. 4: **(a)** Cross section of the *Interior Rotor* actuator with outer and inner radii, R and r, of the actuator stator winding volume, and **(b)** the assumed lumped-parameter steady-state thermal model of the actuator with interior rotor.

i.e. $\hat{\Psi} = N\hat{\Phi}$, and consequently the torque is proportional to $T_{\mathrm{int}} \sim \hat{\Phi} \cdot N\hat{I}_{\mathrm{int}}$. Furthermore, $\hat{\Phi}$ is proportional to the flux density in the air gap B_{ag} and the air gap area A_{ag}, while $N\hat{I}_{\mathrm{int}}$ represents the magnetomotive force, which can be written as the product of the current density amplitude $\hat{J}_{\mathrm{int}}$ and the winding area A_{w}, i.e. $N\hat{I}_{\mathrm{int}} = \hat{J}_{\mathrm{int}} A_{\mathrm{w}}$. Finally, the torque is proportional to $T_{\mathrm{int}} \sim A_{\mathrm{ag}} A_{\mathrm{w}} B_{\mathrm{ag}} \hat{J}_{\mathrm{int}}$.

The air gap and winding areas, A_{ag} and A_{w}, can be further expressed by the geometrical parameters R and r (the outer and inner radii of the winding volume) shown in **Fig. 4(a)**. For the air gap area the expression $A_{\mathrm{ag}} \sim rL$ is applied, where L equals the assumed stator length, and for the winding area the expression $A_{\mathrm{w}} \sim (R^2 - r^2)$ is used. Since in the conducted analysis, the air gap flux density B_{ag} is assumed to be constant, the torque can be scaled as $T_{\mathrm{int}} \sim r(R^2 - r^2)L \cdot \hat{J}_{\mathrm{int}}$ which corresponds with the scaling law deduced in [6]. If a relative parameter $x_{\mathrm{r}} = r/R$ is introduced, the torque is obtained as

$$T_{\mathrm{int}} = K_{\mathrm{T}} \cdot R^3 L \cdot x_{\mathrm{r}}(1 - x_{\mathrm{r}}^2) \cdot \hat{J}_{\mathrm{int}}, \tag{1}$$

where K_{T} is an absolute torque constant that is given in **Tab. III** for the analyzed LiRAs.

As already mentioned, in contrast to the constant current density amplitude $\hat{J}_{\mathrm{int}}$ assumed in [6], in the following a loss-dependent current density $\hat{J}_{\mathrm{int}} = \hat{J}_{\mathrm{int}}(P_{\mathrm{cu}})$ is considered, which is given by the maximum allowed copper losses P_{cu} in the stator windings. Based on the $P_{\mathrm{cu}} = 1/2 R_{\mathrm{cu}} \hat{I}^2_{\mathrm{int}}$, the current density

TABLE II: Parameters used in FEM simulations.

Parameter Name	Value/Expression
Geometrical	
Length (L)	100 mm
Outer Radius (R)	100 mm
Rotor Back Iron Thickness	2 mm
Stator Back Iron Thickness	2 mm
PM Thickness	2 mm
Number of Rotor Poles for Rotation	16(8)*
Number of Rotor Poles for Linear Motion	16(8)*
Number of Stator Teeth for Rotation	6
Number of Stator Teeth for Linear Motion	12
Total LiRA Volume (V)	$\pi R^2 L$
Stator Volume (V_{stator})	$\pi(R^2 - r^2)L$
Relative Winding Radial Size (x_{r})	r/R
Magnetic / Electrical	
PM Remanent Flux Density	1.3 T
Rotor/Stator Core Relative Permeability	10 000
Copper Specific Electric Resistance at T_{w} (ρ_{cu})	$2.36 \times 10^{-8}\,\Omega\,\mathrm{m}$
Relative Copper Volume ($k_{\mathrm{cu}} = V_{\mathrm{cu}}/V_{\mathrm{stator}}$)	0.36
Current Density Constant (K_{J})	$2\sqrt{\Delta T/(\rho_{\mathrm{cu}} k_{\mathrm{cu}})}$
Thermal	
Winding Temperature (T_{w})	120 °C
Ambient Temperature (T_{amb})	40 °C
Temperature Difference (ΔT)	$T_{\mathrm{w}} - T_{\mathrm{amb}}$
Heat Transfer Coefficient (h)	$10\,\mathrm{W\,K^{-1}\,m^{-2}}$
Winding Thermal Conductivity (λ_{w})**	$2\,\mathrm{W\,K^{-1}\,m^{-1}}$
Iron Core Thermal Conductivity (λ_{fe})	$22\,\mathrm{W\,K^{-1}\,m^{-1}}$

*Pole number values for S-{Rotor} are in brackets.
**Measured value, see [17].

can be expressed as $\hat{J}_{\mathrm{int}} = \sqrt{(2P_{\mathrm{cu}})/(\rho_{\mathrm{cu}} V_{\mathrm{cu}})}$, where ρ_{cu} is the specific resistance of copper and V_{cu} the copper volume of the stator, which is given as $V_{\mathrm{cu}} = k_{\mathrm{cu}} V_{\mathrm{stator}}$ (cf. **Tab. II**).

The allowed copper losses P_{cu} are deduced from the actuator's thermal properties, whereby the two heat transfer modes are considered: (1) radial heat flow through the windings by thermal conduction, modelled by the thermal resistance $R^{\mathrm{th}}_{\mathrm{in}}$ and (2) radial heat convection on the outer surface of the actuator to the environment, modelled by the thermal resistance $R^{\mathrm{th}}_{\mathrm{out}}$, which assumes a certain loss per surface area. The two thermal resistances can be obtained as

$$R^{\mathrm{th}}_{\mathrm{in}} = \frac{1}{\lambda_{\mathrm{w}}} \frac{\ln(R/r)}{2\pi L}, \qquad R^{\mathrm{th}}_{\mathrm{out}} = \frac{1}{h} \frac{1}{2\pi R L}, \tag{2}$$

where λ_{w} is the specific thermal conductivity of the winding and h is the heat transfer coefficient from the actuator's outer surface to the environment (cf. **Tab. II**). The assumed thermal model is shown in **Fig. 4(b)**. The allowed copper losses are obtained as $P_{\mathrm{cu}} = \Delta T/(R^{\mathrm{th}}_{\mathrm{in}} + R^{\mathrm{th}}_{\mathrm{out}})$.

The copper volume can be calculated as $V_{\mathrm{cu}} = k_{\mathrm{cu}} \cdot \pi(R^2 - r^2)L$, where k_{cu} is considering the amount of copper volume relative to the total stator volume. Assuming a winding fill factor equal to 0.6 and winding volume to stator volume ratio of 0.6, i.e. 60% while 40% is iron), k_{cu} is calculated as $k_{\mathrm{cu}} = 0.6{\cdot}0.6 = 0.36$ (cf. **Tab. II**).

Accordingly, the current density amplitude is calculated as

$$\hat{J}_{\mathrm{int}} = K_{\mathrm{J}} \cdot \frac{1}{R} \frac{1}{\sqrt{1 - x_{\mathrm{r}}^2}} \frac{1}{\sqrt{\dfrac{\ln(1/x_{\mathrm{r}})}{\lambda_{\mathrm{w}}} + \dfrac{1}{hR}}}, \tag{3}$$

where K_{J} is given in **Tab. II**.

The loss- and geometry-dependent current density $\hat{J}_{\mathrm{int}}$ can now be used in (3), in order to obtain the expression for the loss- and geometry-dependent torque T_{int} of the interior rotor actuator. Another important quantity is the torque density $t_{\mathrm{int}} = T_{\mathrm{int}}/V$, which equals the torque T_{int} divided by the total rotary actuator volume V (cf. **Tab. II**) and results in the following expression

$$t_{\mathrm{int}} = \frac{K_{\mathrm{T}} K_{\mathrm{J}}}{\pi} \cdot x_{\mathrm{r}} \sqrt{1 - x_{\mathrm{r}}^2} \cdot \frac{1}{\sqrt{\dfrac{\ln(1/x_{\mathrm{r}})}{\lambda_{\mathrm{w}}} + \dfrac{1}{hR}}}. \tag{4}$$

The first factor is constant, while the second term only depends on the relative quantity x_{r}. The last factor, which comes from the thermal considerations, depends on both, the relative parameter x_{r} and the absolute parameter R. Additionally, the last factor depends on the thermal parameters λ_{w} and h. In order to examine the influence of these two thermal parameters, the extreme cases when $\lambda_{\mathrm{w}} \to \infty$ or $h \to \infty$ are analyzed. Both cases can be physically interpreted and are shown in **Fig. 5(a)**.

If $\lambda_{\mathrm{w}} \to \infty$, then $R^{\mathrm{th}}_{\mathrm{in}} \to 0$, which means that the temperature drop inside the windings can be neglected. This can be related to the scenario in which the heat transfer coefficient h is low (e.g. natural air cooling), i.e. heat transfer to the ambient is so low such that the temperature drop inside the winding becomes negligible. In this scenario, the torque density t_{int} depends on the absolute value of the outer radius as $t_{\mathrm{int}} \sim \sqrt{R}$ and its maximum is achieved for $x_{\mathrm{r}} = 0.707$ (maximum of the function $x_{\mathrm{r}}\sqrt{1 - x_{\mathrm{r}}^2}$, cf. red curve in **Fig. 5(a)**).

If $h \to \infty$, then $R^{\mathrm{th}}_{\mathrm{out}} \to 0$, which means the case temperature of the actuator is fixed. This corresponds to the scenario where the heat transfer coefficient h would be very high (e.g. water cooling), such that the main temperature drop occurs inside the machine. This is represented with the green curve in **Fig. 5(a)**, which is a monotonically increasing function, since in case the windings get thinner (increasing x_{r}), the thermal resistance $R^{\mathrm{th}}_{\mathrm{in}}$ of the winding in radial direction is decreasing. Consequently,

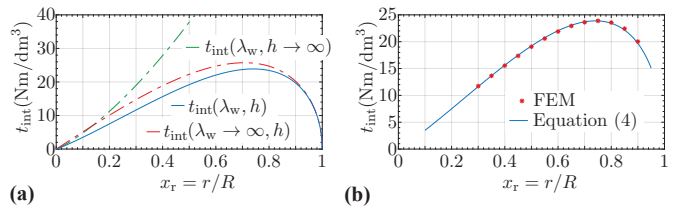

Fig. 5: Scaling law of the achievable torque density for the *Interior Rotor* actuator. **(a)** Overall torque density t_{int} (blue), and for the cases where either $\lambda_{\mathrm{w}} \to \infty$ (red) or $h \to \infty$ (green). **(b)** Verification of the analytically derived torque density t_{int} with FEM simulations. The parameters used in the simulation are given in **Tab. II**.

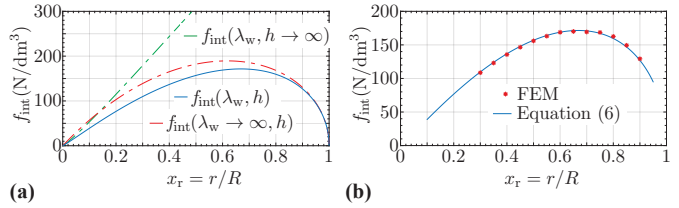

Fig. 6: Scaling law of the achievable force density for the *Interior Rotor* actuator. **(a)** Overall force density f_{int} (blue), and for the cases where either $\lambda_{\mathrm{w}} \to \infty$ (red) or $h \to \infty$ (green). **(b)** Verification of the analytically derived force density f_{int} with FEM simulations. The parameters used in the simulation are given in **Tab. II**.

more copper losses can be dissipated and a higher torque can be generated.

The curve that considers both, inner and outer thermal resistances, is always below the curves of the discussed scenarios (cf. **Fig. 5(a)**), as it is limited by both thermal resistances. This curve is also verified with FEM simulations as shown in **Fig. 5(b)**.

2) Thrust Force Scaling Law: Similar to the torque, the thrust (axial or drive) force F_{int} is proportional to the flux linkage and the 3-phase current amplitude, $F_{\mathrm{int}} \sim \hat{\Psi}\hat{I}_{\mathrm{int}}$ and therefore is proportional to $F_{\mathrm{int}} \sim A_{\mathrm{ag}} A_{\mathrm{w}} B_{\mathrm{ag}} \hat{J}_{\mathrm{int}}$. The air gap and winding areas, A_{ag} and A_{w}, can be deduced by using the geometrical parameters R and r from **Fig. 4(a)**. Similar to the derivation from **Sec. III-A1**, $A_{\mathrm{ag}} \sim rL$, while in the case of a linear actuator, the winding area only depends linearly on the radii and further is independent of the length L, i.e. $A_{\mathrm{w}} \sim (R - r)$. Assuming the air gap flux density B_{ag} to be constant, the force is proportional to $F_{\mathrm{int}} \sim r(R - r)L \cdot \hat{J}_{\mathrm{int}}$, and by using the same relative parameter x_{r}, can be written as

$$F_{\mathrm{int}} = K_{\mathrm{F}} \cdot R^2 L \cdot x_{\mathrm{r}}(1 - x_{\mathrm{r}}) \cdot \hat{J}_{\mathrm{int}}, \tag{5}$$

where K_{F} is an absolute axial force constant that is given in **Tab. III** for the analyzed LiRAs.

The cooling properties are assumed to be the same as in the case of the rotary actuator, thus the current density $\hat{J}_{\mathrm{int}}$ is also given with (3) and can be inserted into (5). Similar to the torque density, the force density f_{int} can be derived by dividing the force F_{int} by the total linear actuator volume V (cf. **Tab. II**), which results in

$$f_{\mathrm{int}} = \frac{K_{\mathrm{F}} K_{\mathrm{J}}}{\pi} \cdot \frac{1}{R} \cdot x_{\mathrm{r}} \sqrt{\frac{1 - x_{\mathrm{r}}}{1 + x_{\mathrm{r}}}} \cdot \frac{1}{\sqrt{\dfrac{\ln(1/x_{\mathrm{r}})}{\lambda_{\mathrm{w}}} + \dfrac{1}{hR}}}. \tag{6}$$

Compared to the torque density in (4), the force density has a factor $1/R$, which means that the force density is increasing with a decreasing actuator's outer radius. Hence, linear actuators (motors) are typically build with rather high length over radius (L/R) ratios.

The last factor in (6), which considers the thermal properties of the machine, is the same as the one in (4), therefore a discussion similar to **Sec. III-A1** is conducted here.

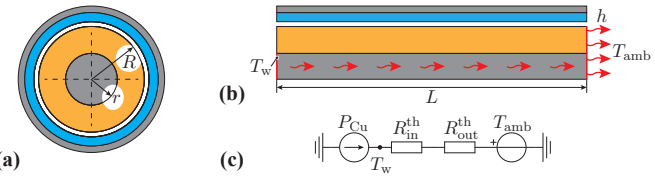

Fig. 7: Tubular linear-rotary actuator with *Exterior Rotor* with **(a)** radial and **(b)** axial cross sections. Based on the axial mounting of the interior stator, only axial heat flow is assumed and denoted with the red arrows. **(c)** Corresponding lumped parameter steady-state thermal model.

If $\lambda_{\mathrm{w}} \to \infty$, the force density depends on the absolute outer radius as $f_{\mathrm{int}} \sim 1/\sqrt{R}$. The influence of the relative parameter x_{r} is reduced to $f_{\mathrm{int}} \sim x_{\mathrm{r}}\sqrt{(1 - x_{\mathrm{r}})/(1 + x_{\mathrm{r}})}$, which is shown in **Fig. 6(a)** with the red curve $f_{\mathrm{int}}(\lambda \to \infty, h)$. In this scenario, the maximum force density is achieved for $x_{\mathrm{r}} = 0.618$.

If $h \to \infty$, the force density depends on the absolute outer radius as $f_{\mathrm{int}} \sim 1/R$, and in addition is again monotonically increasing with the relative parameter x_{r}. Again, the curve that considers both heat transfer coefficients λ_{w} and h is always smaller than the curves where only one of these parameters is considered. The verification with FEM simulations is shown in **Fig. 6(b)**.

B. Exterior Rotor

1) Torque Scaling Law: In analogy to the actuator with interior rotor, the torque T_{ext} of the actuator with exterior rotor is proportional to $T_{\mathrm{ext}} \sim A_{\mathrm{ag}} A_{\mathrm{w}} B_{\mathrm{ag}} \hat{J}_{\mathrm{ext}}$. Based on the geometric dimensions given in **Fig. 7**, the air gap area can be expressed by $A_{\mathrm{ag}} \sim RL$, and the winding area by $A_{\mathrm{w}} \sim (R^2 - r^2)$. Moreover, with a constant air gap flux density B_{ag}, the torque is calculated as $T_{\mathrm{ext}} \sim R(R^2 - r^2)L \cdot \hat{J}_{\mathrm{ext}}$. Finally, using the relative parameter $x_{\mathrm{r}} = r/R$, the torque becomes

$$T_{\mathrm{ext}} = K_{\mathrm{T}} \cdot R^3 L \cdot (1 - x_{\mathrm{r}}^2) \cdot \hat{J}_{\mathrm{ext}}, \tag{7}$$

where K_{T} is again the absolute torque constant given in **Tab. III**.

For the exterior rotor actuator, i.e. interior stator actuator, the stator can only be mechanically fixed at one of the axial ends, therefore leading to an axial heat flow in the actuator (cf. **Fig. 7(b)**). The end with the mechanical fixation is assumed to have a heatsink with an area equal to πR^2 and a heat transfer coefficient h, which results in an outer thermal resistance $R^{\mathrm{th}}_{\mathrm{out}}$ (cf. **Fig. 7(c)**). Accordingly, due to the axial heat flow, the hot spot temperature is on the opposite axial end, with the temperature T_{w} (cf. **Fig. 7(b)**). It is assumed that the axial heat flow occurs only in the stator back iron (cylinder with the radius r), while it is neglected through the winding volume, since the thermal conductivity in the winding is mainly inhibited by the poor conductance of the wire isolation and potting material ($\lambda_{\mathrm{fe}}/\lambda_{\mathrm{w}} \sim 10$). Furthermore, as the copper losses P_{cu} are distributed in the winding volume, the heat generation is also spatially distributed along the stator, resulting in an inner thermal resistance $R^{\mathrm{th}}_{\mathrm{in}}$ to be half of the total back iron's thermal resistance $R^{\mathrm{th}}_{\mathrm{fe}}$, i.e. $R^{\mathrm{th}}_{\mathrm{in}} = R^{\mathrm{th}}_{\mathrm{fe}}/2$. Accordingly, the thermal resistances for the tubular actuator with the exterior rotor can be calculated as

$$R^{\mathrm{th}}_{\mathrm{in}} = \frac{1}{2\lambda_{\mathrm{fe}}} \frac{L}{\pi r^2}, \qquad R^{\mathrm{th}}_{\mathrm{out}} = \frac{1}{h} \frac{1}{\pi R^2}, \tag{8}$$

where λ_{fe} is the thermal conductivity of iron given in **Tab. II**. Applying the same considerations as in **Sec. III-A1**, the allowed current density is obtained as

$$\hat{J}_{\mathrm{ext}} = K_{\mathrm{J}} \cdot \frac{1}{\sqrt{L}} \cdot \frac{1}{\sqrt{1 - x_{\mathrm{r}}^2}} \cdot \frac{1}{\sqrt{\dfrac{1}{\lambda_{\mathrm{fe}}} \dfrac{L}{x_{\mathrm{r}}^2} + \dfrac{2}{h}}}, \tag{9}$$

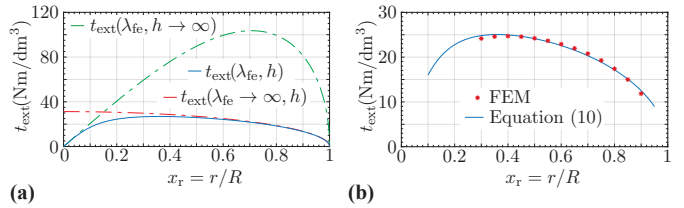

Fig. 8: Scaling law of the achievable torque for the *Exterior Rotor* actuator **(a)** Overall torque density t_{ext} (blue), and influence of the thermal parameters λ_{fe} (red) and h (green) onto the torque density t_{ext}. **(b)** Torque density t_{ext} verified with FEM simulation with parameters given in **Tab. II**.

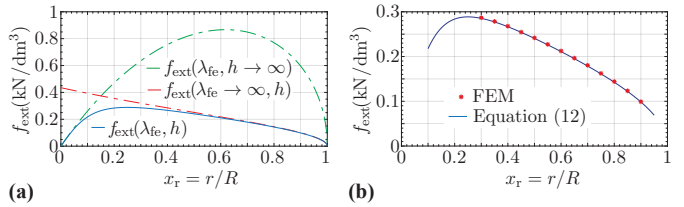

Fig. 9: Scaling law of the achievable force for the *Exterior Rotor* actuator **(a)** Overall force density f_{ext} (blue), and influence of the thermal parameters λ_{fe} (red) and h (green) onto the force density f_{ext}. **(b)** Force density f_{ext} verified with FEM simulations with parameters given in **Tab. II**.

where K_{J} is given in **Tab. II**. Inserting this equation into (7) and dividing it by the rotary actuator volume V (cf. **Tab. II**), the following expression is obtained for the torque density

$$t_{\text{ext}} = \frac{K_{\text{T}} K_{\text{J}}}{\pi} \cdot \frac{R}{\sqrt{L}} \cdot \sqrt{1 - x_{\text{r}}^2} \cdot \frac{1}{\sqrt{\frac{1}{\lambda_{\text{fe}}} \frac{L}{x_{\text{r}}^2} + \frac{2}{h}}}. \tag{10}$$

As can be noticed, the torque density t_{ext} depends on the ratio of the absolute outer dimensions R and L, which means that making the actuator longer, reduces the torque density due to the worse axial heat flow. Similarly to **Sec. III-A1**, the two extreme scenarios $h \to \infty$ or $\lambda_{\text{fe}} \to \infty$ can be analyzed (cf. **Fig. 8(b)**).

Again, the scaling law considering both thermal parameters is verified with FEM simulations as shown in **Fig. 8(b)**.

2) Thrust Force Scaling Law: In analogy to the derivation done for the interior rotor, the thrust force F_{ext} is given as $F_{\text{ext}} \sim A_{\text{ag}} A_{\text{w}} B_{\text{ag}} \hat{J}_{\text{ext}}$. The air gap and the winding areas are again proportional to $A_{\text{ag}} \sim RL$ and $A_{\text{w}} \sim (R - r)$ and with the assumption of a constant air gap flux density B_{ag}, the force is proportional to $F_{\text{ext}} \sim R(R-r)L \cdot \hat{J}_{\text{ext}}$. By using $x_{\text{r}} = r/R$, the previous expression can be written as

$$F_{\text{ext}} = K_{\text{F}} \cdot R^2 L \cdot (1 - x_{\text{r}}) \cdot \hat{J}_{\text{ext}}, \tag{11}$$

where K_{F} is the force constant and the current density is given with (9). Hence, the force density for the tubular actuator with exterior rotor is obtained as

$$f_{\text{ext}} = \frac{K_{\text{F}} K_{\text{J}}}{\pi} \cdot \frac{1}{\sqrt{L}} \cdot \sqrt{\frac{1 - x_{\text{r}}}{1 + x_{\text{r}}}} \cdot \frac{1}{\sqrt{\frac{1}{\lambda_{\text{fe}}} \frac{L}{x_{\text{r}}^2} + \frac{2}{h}}}. \tag{12}$$

The force density f_{ext} only depends on the absolute length L and decays when the length L of the actuator increases. This effect is pronounced due to the axial heat flow in the actuator. The influence of the thermal parameters λ_{fe} and h is analyzed and shown in **Fig. 9(a)**, while the verification by FEM simulation is shown in **Fig. 9(b)**.

In general, for the tubular actuator with exterior rotor and therefore internal axial heat flow, the consideration of the thermal aspects is very important, since they influence the actuator geometry significantly as shown in **Fig. 8(a)** and **Fig. 9(a)**.

TABLE III: Scaling law constants determined by FEM simulations.

Rotor	Stator	K_{T} (N A^{-1} m^{-3})	K_{F} (N A^{-1} m^{-2})
Interior Rotor			
R	R	0.83	-
S	R	0.35	-
L	L	-	0.93
S	L	-	0.48
Exterior Rotor			
R	R	0.71	-
L	L	-	0.99

C. Scaling Law Constants

In this section, the absolute values of the scaling law constants K_{T} and K_{F} are given and briefly discussed. **Tab. III** summarizes the constants for the actuators with {R,L,S}-Rotor and {R,L}-Stator for the interior rotor and with {R,L}-Rotor and {R,L}-Stator for the exterior rotor. The actuator constants for the rest of the actuator arrangements from **Fig. 3** will be analyzed in future work.

As intuitively expected, the actuator constants for the S-Rotor are around 2 times lower compared to the R-Rotor and L-Rotor. This is the consequence of the 2 times lower PM cross section area, and therefore around 2 times lower flux linkage. More detailed analysis of the S-Rotor and its application in high dynamic positioning systems is explained in [10].

IV. Design Example Discussion

As an example, in this section, the two possible realization options of the LiRA-1 (MB, L, R, MB) with interior rotor are compared, i.e. where either a combination of an L- and R-Rotor or a S-Rotor is used (cf. **Fig. 1** and **Fig. 3**). In a first step, the magnetic bearings are not considered, since on the one hand the MBs are not yet considered in the scaling laws, and on the other hand the scaling laws are also applicable to machines with conventional bearings. Furthermore, the design discussion is conducted for the dimensions also used for the FEM simulations as given in **Tab. II**. Thereby, the length L equals the total length of the complete actuator, which means that the axial stroke (Δz), the rotary actuator length L_{R} and the linear actuator length L_{L} have to be accommodated in the total length L. As already discussed, for the combined LR-Rotor the distance Δz between the linear and rotary machines must be at least as large as the specified maximum stroke z_{stroke}, while for the S-Rotor no distance between the machines is needed ($\Delta z = 0$). However, it also must be mentioned that with the S-Rotor lower torque and force constants are achieved (cf. **Tab. III**), and therefore the volumes of the rotary machine V_R and linear machine volume V_L are bigger in order to achieve the same absolute torques and forces. Hence, considering the volume between the machines defined by Δz as additional actuator volume V_z, the question arises for which range of stroke z_{stroke} which machine realization results in a smaller overall actuator volume V_A if a given absolute torque T and force F must be achieved. The total actuator volume is actually defined as $V_A = V_R + V_L + V_z$, which, based on the assumption of a constant outer radius R for all machines, corresponds to $L = L_R + L_L + \Delta z$. Accordingly, in case of the RL-Rotor with increasing Δz, the remaining length for L_R and L_L is reduced, which in consequence also leads to a reduction of the maximum achievable force and torque performance, while for the S-Rotor always the full actuator length L can be shared between the two machines. Moreover, for both actuator realizations, the length distribution between L_R and L_L can be selected arbitrarily. E.g. in the extreme case, where $L_L = 0$ and $L_R = L - \Delta z$, the actuator achieves the maximum torque but no axial force is obtained, i.e. only a rotary machine. However, if now L_R is decreased, also the maximum achievable torque decreases linearly, since $T = t \cdot V_R \sim t \cdot L_R$, and the axial force linearly increases, since $F = f \cdot V_L \sim f \cdot L_L$.

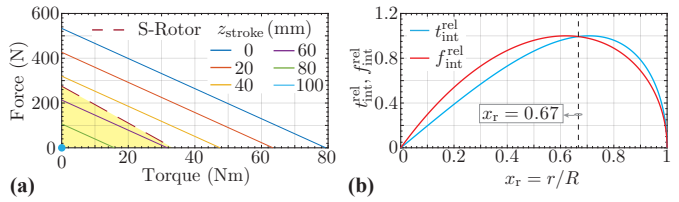

Fig. 10: (a) Achievable absolute forces and torques of the LiRA-1 with interior rotor arrangement for different lengths of stroke z_{stroke}. The performance of the LiRA-1 with combined LR-Rotor depends on the stroke (solid lines), while it it is independent from the stroke when realized with a S-Rotor. **(b)** Determining the relative parameter x_{r} by using the normalized torque and force densities $t_{\text{int}}^{\text{rel}} = t_{\text{int}}/\max(t_{\text{int}})$ and $f_{\text{int}}^{\text{rel}} = f_{\text{int}}/\max(f_{\text{int}})$. For the LR-rotor the optimum radius ratios are found at $x_{\text{r}} = 0.711$ for rotary machine and at $x_{\text{r}} = 0.624$ for the linear machine. For the S-Rotor a sub-optimal value of $x_{\text{r}} = 0.67$ is selected, which however for the given dimensions hardly decreases the achievable torque and force densities.

This behavior is visualized in **Fig. 10(a)** for different stroke lengths z_{stroke}. As can be clearly noticed, for the LR-Rotor, the achievable torque-force-ratio decreases with increasing z_{stroke} and for a maximum stroke of $z_{\text{stroke}} = 100\,\text{mm}$ neither an axial force nor a torque can be achieved. On the other hand, for the S-Rotor, a stroke-independent torque-force-ratio is obtained. In this case, the break even in performance is roughly found at the half of the total actuator length $L/2 = 50\,\text{mm}$, which means that for axial strokes smaller than $L/2$ the LR-Rotor performs better, while for $z_{\text{stroke}} > L/2$ the S-Rotor should be used (cf. yellow shaded area in **Fig. 10(b)**). The factor $1/2$ actually comes from the ratio of the torque and force constants K_{T} and K_{F}, which for the two rotor type roughly differs by this factor. Hence, z_{stroke} of the break-even point can easily be estimated by writing $L_{R,LR}+L_{L,LR}+\Delta z = L_{R,S}+L_{L,S}+\Delta z$, where $K_{T,LR} \cdot L_{R,LR} = K_{T,S} \cdot L_{R,S}$ and $K_{F,LR} \cdot L_{F,LR} = K_{F,LR} \cdot L_{R,S}$ must be guaranteed in order to achieve the same absolute torque and force values. For the sake of completeness, it must be mentioned that also the relative parameter x_{r} can strongly influence this break-even point, since for the combined LR-Rotor both machines can be designed independently, which means that the rotor radius r can be optimized for each machine, i.e. always the optimum x_{r} can be selected, while for the S-Rotor the same x_{r} for both machine must be used. This is explained by **Fig. 10(b)**, where the two normalized torque and force densities, achievable for the specifications given **Tab. II**, in are shown. Accordingly, the LR-rotor would be realized with two different diameters, where for the rotary machine the optimum radius ratio is $x_{\text{r}} = 0.711$ and for the linear machine $x_{\text{r}} = 0.624$. For the S-rotor a compromise between torque and force has to be made, which for the given actuator dimensions is found at $x_{\text{r}} = 0.67$. As can be noticed, this sub-optimal radius ratio is hardly decreasing the achievable force and torque densities, however, for other actuator dimensions can be much larger, which means that the break-even point concerning achievable performance is shifted to even larger strokes z_{stroke}.

Conclusions

This paper gives an overview of possible realization concepts to build a linear-rotary actuator (LiRAs) with magnetic bearings (MB), i.e. a self-bearing electric machine that can realize coupled linear and rotary movements. In order to help the designer to easily compare different realization options and to simplify the selection of the appropriate actuator concept for a given application, general scaling laws concerning torque and forces considering also the heat flow inside and outside the actuator are deduced for interior and exterior rotor arrangements. All the findings are verified with FEM simulations. The scaling laws are also applicable to special actuators (checkerboard or double-stator) as well as to standard rotary and/or linear actuators with conventional bearings, as was also done for a design example in this paper. The comparison of linear-rotary actuator realized with either separate linear and rotary machines or a combined linear-rotary machine showed, that the separate realization outperforms the combined actuator with respect to the total actuator volume as long as the linear stroke is smaller than half the length of the total actuator. Furthermore, depending on the outer dimensions given by the underlying application, this break-even point can be even shifted to larger stroke values, since for the separate realization both machines can be optimized independently, while for the combined actuator a compromise has to be made. The future work will focus onto further development of the scaling laws and the comparison of the further LiRA arrangements.

Acknowledgment

This work was supported by ETH Research Grant ETH-13 16-2. The authors would like to acknowledge the support of CADFEM (Suisse) AG concerning the ANSYS software package. Warm thanks also go to Marcel Schuck for the useful suggestions when writing the digest of this paper.

References

[1] K. J. Meessen, J. J. Paulides, and E. A. Lomonova, "Modeling and Experimental Verification of a Tubular Actuator for 20-g Acceleration in a Pick-and-Place Application," *IEEE Transactions on Industry Applications*, vol. 46, no. 5, pp. 1891–1898, 2010.

[2] L. Xie, J. Si, Y. Hu, and Z. Wang, "Overview of 2-Degree-of-Freedom Rotary-Linear Motors Focusing on Coupling Effect," *IEEE Transactions on Magnetics*, 2019.

[3] K. Guo and Y. Guo, "Key Parameter Design and Analysis of Flux Reversal Linear Rotary Permanent Magnet Actuator," *IEEE Transactions on Applied Superconductivity*, vol. 29, no. 2, pp. 1–5, 2019.

[4] T. Yamasaki, "Electric Linear Motion Actuator and Electric Brake System," 2019, US Patent App. 10/215,265.

[5] W. Lee, S. Li, D. Han, B. Sarlioglu, T. A. Minav, and M. Pietola, "A Review of Integrated Motor Drive and Wide-Bandgap Power Electronics for High-Performance Electro-Hydrostatic Actuators," *IEEE transactions on transportation electrification*, vol. 4, no. 3, pp. 684–693, 2018.

[6] T. Reichert, T. Nussbaumer, and J. W. Kolar, "Torque Scaling Laws for Interior and Exterior Rotor Permanent Magnet Machines," in *Proc. of IEEE International Magnetics Conference (INTERMAG)*, 2009, pp. 1–4.

[7] K. Meessen, J. Paulides, and E. Lomonova, "Analysis and Design Considerations of a 2-DoF Rotary-Linear Actuator," in *Proc. of IEEE International Electric Machines & Drives Conference (IEMDC)*, 2011, pp. 336–341.

[8] P. Jin, H. Lin, S. Fang, Y. Yuan, Y. Guo, and Z. Jia, "3-D Analytical Linear Force and Rotary Torque Analysis of Linear and Rotary Permanent Magnet Actuator," *IEEE Transactions on Magnetics*, vol. 49, no. 7, pp. 3989–3992, 2013.

[9] G. Krebs, A. Tounzi, B. Pauwels, D. Willemot, and M. Piriou, "Design of a Permanent Magnet Actuator for Linear and Rotary Movements," *The European Physical Journal-Applied Physics*, vol. 44, no. 1, pp. 77–85, 2008.

[10] S. Mirić, M. Schuck, A. Tüysüz, and J. W. Kolar, "Double Stator Linear-Rotary Actuator with a Single Set of Mover Magnets," in *Proc. of IEEE Energy Conversion Congress and Exposition (ECCE USA)*, 2018, pp. 750–757.

[11] A. Schleicher and R. Werner, "Theoretical and Experimental Analysis of Controllability of a Novel Bearingless Rotary-Linear Reluctance Motor with Optimal Chessboard Toothing," in *Proc. of IEEE International Conference on Industrial Technology (ICIT)*, 2018, pp. 540–545.

[12] N.-C. Tsai and C.-W. Chiang, "Design and Analysis of Magnetically-Drive Actuator Applied for Linear Compressor," *Mechatronics*, vol. 20, no. 5, pp. 596–603, 2010.

[13] S. Mirić, P. Küttel, A. Tüysüz, and J. W. Kolar, "Design and Experimental Analysis of a New Magnetically Levitated Tubular Linear Actuator," *IEEE Transactions on Industrial Electronics*, vol. 66, no. 6, pp. 4816–4825, 2019.

[14] L. Xu, M. Lin, X. Fu, and N. Li, "Design and Analysis of a Double-Stator Linear-Rotary Permanent-Magnet Motor," *IEEE Transactions on Applied Superconductivity*, vol. 26, no. 4, pp. 1–4, 2016.

[15] T. Baumgartner and J. W. Kolar, "Multivariable State Feedback Control of a 500 000-r/min Self-Bearing Permanent-Magnet Motor," *IEEE/ASME Transactions on Mechatronics*, vol. 20, no. 3, pp. 1149–1159, 2015.

[16] S. Mirić, A. Tüysüz, and J. W. Kolar, "Comparative Evaluation of Linear-Rotary Actuator Topologies for Highly Dynamic Applications," in *Proc. of IEEE International Electric Machines and Drives Conference (IEMDC)*, 2017, pp. 1–7.

[17] N. Simpson, R. Wrobel, and P. H. Mellor, "Estimation of Equivalent Thermal Parameters of Impregnated Electrical Windings," *IEEE Transactions on Industry Applications*, vol. 49, no. 6, pp. 2505–2515, 2013.